# Measurement of inclusive production of $\eta$, $\eta\prime$ and $\phi$ mesons in $D^0$, $D^+$ and $D_s^+$ decays

G. S. Huang,[1] D. H. Miller,[1] V. Pavlunin,[1] B. Sanghi,[1] I. P. J. Shipsey,[1] B. Xin,[1] G. S. Adams,[2] M. Anderson,[2] J. P. Cummings,[2] I. Danko,[2] J. Napolitano,[2] Q. He,[3] J. Insler,[3] H. Muramatsu,[3] C. S. Park,[3] E. H. Thorndike,[3] F. Yang,[3] T. E. Coan,[4] Y. S. Gao,[4] M. Artuso,[5] S. Blusk,[5] J. Butt,[5] J. Li,[5] N. Menaa,[5] R. Mountain,[5] S. Nisar,[5] K. Randrianarivony,[5] R. Sia,[5] T. Skwarnicki,[5] S. Stone,[5] J. C. Wang,[5] K. Zhang,[5] S. E. Csorna,[6] G. Bonvicini,[7] D. Cinabro,[7] M. Dubrovin,[7] A. Lincoln,[7] D. M. Asner,[8] K. W. Edwards,[8] R. A. Briere,[9] J. Chen,[9] T. Ferguson,[9] G. Tatishvili,[9] H. Vogel,[9] M. E. Watkins,[9] J. L. Rosner,[10] N. E. Adam,[11] J. P. Alexander,[11] K. Berkelman,[11] D. G. Cassel,[11] J. E. Duboscq,[11] K. M. Ecklund,[11] R. Ehrlich,[11] L. Fields,[11] R. S. Galik,[11] L. Gibbons,[11] R. Gray,[11] S. W. Gray,[11] D. L. Hartill,[11] B. K. Heltsley,[11] D. Hertz,[11] C. D. Jones,[11] J. Kandaswamy,[11] D. L. Kreinick,[11] V. E. Kuznetsov,[11] H. Mahlke-Krüger,[11] P. U. E. Onyisi,[11] J. R. Patterson,[11] D. Peterson,[11] J. Pivarski,[11] D. Riley,[11] A. Ryd,[11] A. J. Sadoff,[11] H. Schwarthoff,[11] X. Shi,[11] S. Stroiney,[11] W. M. Sun,[11] T. Wilksen,[11] M. Weinberger,[11] S. B. Athar,[12] R. Patel,[12] V. Potlia,[12] J. Yelton,[12] P. Rubin,[13] C. Cawlfield,[14] B. I. Eisenstein,[14] I. Karliner,[14] D. Kim,[14] N. Lowrey,[14] P. Naik,[14] C. Sedlack,[14] M. Selen,[14] E. J. White,[14] J. Wiss,[14] R. E. Mitchell,[15] M. R. Shepherd,[15] D. Besson,[16] T. K. Pedlar,[17] D. Cronin-Hennessy,[18] K. Y. Gao,[18] J. Hietala,[18] Y. Kubota,[18] T. Klein,[18] B. W. Lang,[18] R. Poling,[18] A. W. Scott,[18] A. Smith,[18] P. Zweber,[18] S. Dobbs,[19] Z. Metreveli,[19] K. K. Seth,[19] A. Tomaradze,[19] J. Ernst,[20] H. Severini,[21] S. A. Dytman,[22] W. Love,[22] V. Savinov,[22] O. Aquines,[23] Z. Li,[23] A. Lopez,[23] S. Mehrabyan,[23] H. Mendez,[23] and J. Ramirez[23]

(CLEO Collaboration)

[1]*Purdue University, West Lafayette, Indiana 47907, USA*
[2]*Rensselaer Polytechnic Institute, Troy, New York 12180, USA*
[3]*University of Rochester, Rochester, New York 14627, USA*
[4]*Southern Methodist University, Dallas, Texas 75275, USA*
[5]*Syracuse University, Syracuse, New York 13244, USA*
[6]*Vanderbilt University, Nashville, Tennessee 37235, USA*
[7]*Wayne State University, Detroit, Michigan 48202, USA*
[8]*Carleton University, Ottawa, Ontario, Canada K1S 5B6*
[9]*Carnegie Mellon University, Pittsburgh, Pennsylvania 15213, USA*
[10]*Enrico Fermi Institute, University of Chicago, Chicago, Illinois 60637, USA*
[11]*Cornell University, Ithaca, New York 14853*
[12]*University of Florida, Gainesville, Florida 32611, USA*
[13]*George Mason University, Fairfax, Virginia 22030, USA*
[14]*University of Illinois, Urbana-Champaign, Illinois 61801, USA*
[15]*Indiana University, Bloomington, Indiana 47405, USA*
[16]*University of Kansas, Lawrence, Kansas 66045, USA*
[17]*Luther College, Decorah, Iowa 52101, USA*
[18]*University of Minnesota, Minneapolis, Minnesota 55455, USA*
[19]*Northwestern University, Evanston, Illinois 60208, USA*
[20]*State University of New York at Albany, Albany, New York 12222, USA*
[21]*University of Oklahoma, Norman, Oklahoma 73019, USA*
[22]*University of Pittsburgh, Pittsburgh, Pennsylvania 15260, USA*
[23]*University of Puerto Rico, Mayaguez, Puerto Rico 00681*

(Received 4 October 2006; published 28 December 2006)

We measure the inclusive branching fractions of charm mesons into three mesons with large $s\bar{s}$ content, namely, the $\eta$, $\eta'$ and $\phi$. Data were accumulated with the CLEO-c detector. For $D^0$ and $D^+$ rates, we use 281 pb$^{-1}$ taken on the $\psi(3770)$ resonance, and for $D_s^+$ rates, we use 195 pb$^{-1}$ taken at 4170 MeV. We find that the production rates of these particles are larger in $D_s^+$ decays than in $D^0$ and $D^+$ decays. The $\phi$ rate, in particular, is 15 times greater. These branching fractions can be used to measure $B_s$ yields either at the $\Upsilon(5S)$ resonance or at hadron colliders.

DOI: 10.1103/PhysRevD.74.112005 PACS numbers: 13.20.Fc, 13.66.Bc

 

## I. INTRODUCTION

Inclusive decay rates of charm mesons into mesons with large $s\bar{s}$ inherent quark content, the $\eta$, $\eta'$ and $\phi$ mesons, are important for studies of both charm and $b$ decays. Nonstrange $D$ mesons are generally expected not to decay into such objects, while the $D_s^+$ is likely to have both $s$ and $\bar{s}$ quarks present after the primary $c \to sW^+$ transition, resulting in many more such particles. This is particularly useful in distinguishing between $B$ and $B_s$ mesons as the $B$ decays into $D$'s with a large rate of $\sim$90%, while the decays into $D_s^+$ are at the $\sim$10% level. We expect that the reverse is true for $B_s$ mesons. Knowledge of the charm yields into these mesons would allow alternative analyses of $B_s$ rates at the $\Upsilon(5S)$ or at hadron colliders [1].

In this analysis we use 281 pb$^{-1}$ integrated luminosity of CLEO-c data produced in $e^+e^-$ collisions and recorded at the peak of the $\psi''$ resonance (3.770 GeV) to study the $\eta$, $\eta'$ and $\phi$ yields in $D^0$ and $D^+$ decays. Production in $D_s^+$ decays is studied at 4170 MeV, where the cross-section for $D_s^{*\pm}D_s^{\mp}$ is $\sim$1 nb [2].

The CLEO-c detector is equipped to measure the momenta and directions of charged particles, identify charged hadrons, detect photons, and determine with good precision their directions and energies. It has been described in more detail previously [3–5].

## II. SELECTION OF $\bar{D}^0$, $D^-$ AND $D_s^-$ TAGGING MODES

Fully reconstructed charged or neutral $D$ meson candidates are selected from the data at 3.770 GeV, where pairs of $D^0\bar{D}^0$ or $D^+D^-$ mesons are produced. The decay modes used are listed in Table I. In general, in this paper, $D$ refers to either a $D^0$ or $D^+$ meson and its antiparticle, and $D_s$ refers to $D_s^+$ meson and its antiparticle. (Also, mention of a flavor specific state also implies use of the charge-conjugate state.)

At 4.170 GeV [2] we produce $D_s^+D_s^-$ pairs, with one of the $D_s$ being, most of the time, the daughter of a $D_s^*$ decay. Fully reconstructed $D_s^+$ candidates are selected in the decay modes listed in Table II. $D$ mesons at this energy are a source of background, they are mostly produced in $D^*\bar{D}^*$ final states, with a cross-section of $\sim$5 nb, and $D^*\bar{D} + D\bar{D}^*$ final states, with a cross-section of $\sim$2 nb. $D\bar{D}$ is a relatively small, $\sim$2 nb. There also appears to be $D\bar{D}$ production with extra pions.

We fully reconstruct one of the $D$ mesons at 3.770 GeV or one of the $D_s$ mesons at 4.170 GeV to form a specific tag, and then look for cases where the particle produced in association with our tag has a decay of either $\eta \to \gamma\gamma$, $\eta' \to \pi^+\pi^-\eta$, $\eta \to \gamma\gamma$, or $\phi \to K^+K^-$.

All acceptable track candidates must have a helical trajectory that approaches the event origin within a distance of 5 mm in the azimuthal projection and 5 cm in the polar view, where the azimuthal projection is in the bend view of the solenoidal magnet. Each track must possess at least 50% of the hits expected to be on a track, and it must be within the fiducial volume of the drift chambers, $|\cos\theta| < 0.93$, where $\theta$ is the polar angle with respect to the beam direction.

We reconstruct $\pi^0$'s by first selecting photon candidates from energy deposits in the crystals that are not matched to charged tracks and that have deposition patterns consistent with that expected for electromagnetic showers. Pairs of photon candidates are kinematically fit to the known $\pi^0$ mass [6]. We require the pull, the difference between the reconstructed and known $\pi^0$ mass normalized by its uncertainty, to be less than three for acceptable $\pi^0$ candidates.

$K_S$ candidates are formed from a pair of charged pions that are constrained to come from a single vertex. We also require that the invariant mass of the two pions be within 4.5 times the width of the $K_S$ mass peak, which has an r.m.s. width of 4 MeV.

TABLE I. Tagging modes and numbers of signal and background events determined from the fits to the $D^-$ and $\bar{D}^0$ beam-constrained mass distributions, after making the mode-dependant $m_{\rm BC}$ cuts. The error on the summed signal yield is obtained by adding the errors on the individual yields in quadrature.

| Mode | Signal | Background |
|---|---|---|
| $K^+\pi^-\pi^-$ | 77387 ± 281 | 1868 |
| $K^+\pi^-\pi^-\pi^0$ | 24850 ± 214 | 12825 |
| $K_S\pi^-$ | 11162 ± 136 | 514 |
| $K_S\pi^-\pi^-\pi^+$ | 18176 ± 255 | 8976 |
| $K_S\pi^-\pi^0$ | 20244 ± 170 | 5223 |
| Sum $D^-$ | 151819 ± 487 | 29406 |
| $K^+\pi^-$ | 49418 ± 246 | 630 |
| $K^+\pi^-\pi^0$ | 101960 ± 476 | 18307 |
| $K^+\pi^-\pi^+\pi^-$ | 76178 ± 306 | 6421 |
| Sum $\bar{D}^0$ | 227556 ± 617 | 25357 |

TABLE II. Tagging modes for $D_s^-$ candidates and numbers of signal and background events determined from the fits shown in Fig. 4, after making the mode-dependant invariant mass cuts. The error on the summed signal yield is obtained by adding the errors on the individual yields in quadrature.

| Mode | Signal | Background |
|---|---|---|
| $K^+K^-\pi^-$ | 8446 ± 160 | 6793 |
| $K_SK^-(K_S \to \pi^+\pi^-)$ | 1852 ± 62 | 1022 |
| $\eta\pi^-$ | 1101 ± 80 | 2803 |
| $\eta'\pi^-$ | 786 ± 37 | 242 |
| $\phi\rho^-$ | 1140 ± 59 | 1515 |
| $K^{*+}(890)K^{*0}(890)$ | 1197 ± 81 | 2599 |
| Sum | 14522 ± 218 | 15328 |

We use both charged particle ionization loss in the drift chamber ($dE/dx$) and Ring-Imaging Cherenkov (RICH) information to identify kaons and pions used to fully reconstruct $D$ and $D_s$ mesons. The RICH is used for momenta above 0.7 GeV/$c$. The angle of detected Cherenkov photons that were radiated by a particular charged track are translated into an overall likelihood denoted by $\mathcal{L}_i$ for each particle hypothesis. To differentiate between pion and kaon candidates, we require the difference $-2\log(\mathcal{L}_\pi) + 2\log(\mathcal{L}_K)$ to be less than zero. To utilize the $dE/dx$ information, we calculate $\sigma_\pi$ as the difference between the expected ionization loss for a pion and the measured loss divided by the measurement error. Similarly, $\sigma_K$ is defined using the expected ionization for a kaon.

We use both the RICH and $dE/dx$ information for $D$ and $D_s$ meson tag candidate tracks in the following manner: (a) If neither the RICH nor $dE/dx$ information is available, then the track is accepted as both a pion and a kaon candidate. (b) If $dE/dx$ is available and RICH is not then we insist that pion candidates have $PID_{dE} \equiv \sigma_\pi^2 - \sigma_K^2 < 0$, and kaon candidates have $PID_{dE} > 0$. (c) If RICH information is available and $dE/dx$ is not available, then we require that $PID_{\mathrm{RICH}} \equiv -2\log(\mathcal{L}_\pi) + 2\log(\mathcal{L}_K) < 0$ for pions and $PID_{\mathrm{RICH}} > 0$ for kaons. (d) If both $dE/dx$ and RICH information are available, we require that $(PID_{dE} + PID_{\mathrm{RICH}}) < 0$ for pions and $(PID_{dE} + PID_{\mathrm{RICH}}) > 0$ for kaons.

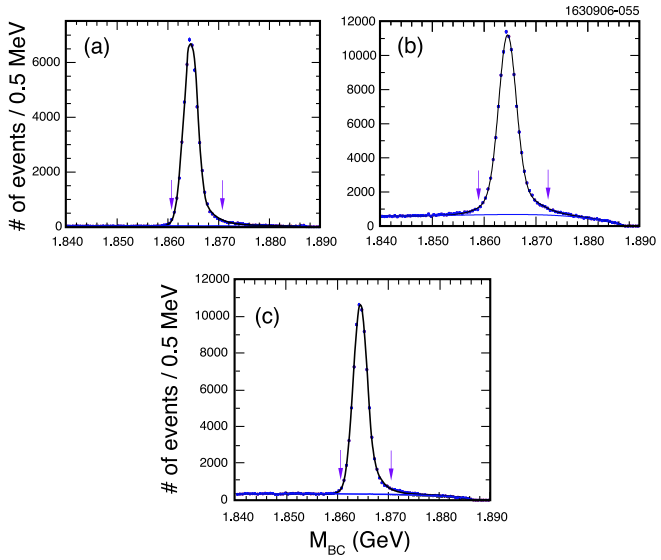


FIG. 1 (color online). Beam-constrained mass distributions for fully reconstructed $\bar{D}^0$ decay candidates in the final states: (a) $K^+\pi^-$, (b) $K^+\pi^-\pi^0$, and (c) $K^+\pi^-\pi^-\pi^+$. The distributions are fit to a Crystal Ball Line shape for the signal. For the background, we either use a fourth order polynomial (in (a) and (b)) or an ARGUS shape (in (c)). Both background shapes are obtained from the $\Delta E$ sidebands. The regions between the arrows are selected for further analysis.

### A. Reconstruction of $\bar{D}^0$ and $D^-$ Tagging Modes

Tagging modes for $D^0$ and $D^+$ decays are reconstructed as described previously [7]. Briefly, at the $\psi(3770)$ $D$ meson final states are reconstructed by first evaluating the difference, $\Delta E$, between the energy of the decay products and the beam energy. We fit the $\Delta E$ spectrum with a double Gaussian to represent the signal, and a polynomial representing the background. We require the absolute value of this difference to contain 98.8% of the signal events, i. e. to be within ~2.5 times the r.m.s width of the peak value. For final states consisting entirely of tracks, the $\Delta E$ resolution is ~7 MeV. A $\pi^0$ in the final state degrades this resolution by roughly a factor of 2. Candidates with $\Delta E$ consistent with zero are selected, and then the $D$ beam-constrained mass is evaluated,

$$m_{\mathrm{BC}} = \sqrt{E_{\mathrm{beam}}^2 - \left(\sum_i \vec{p}_i\right)^2}, \qquad (1)$$

where $i$ runs over all the final state particles.

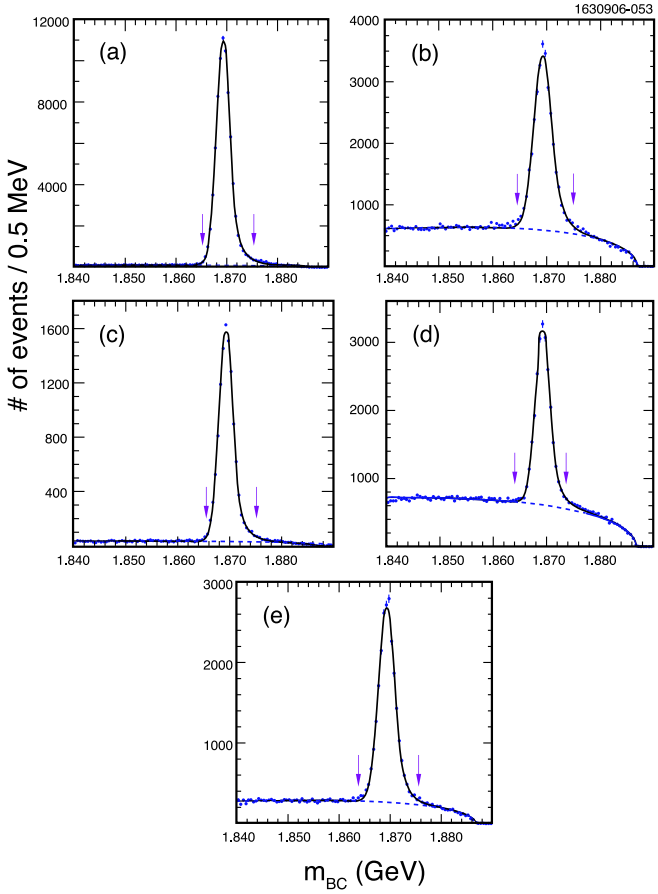


FIG. 2 (color online). Beam-constrained mass distributions for fully reconstructed $D^-$ decay candidates in the final states: (a) $K^+\pi^-\pi^-$, (b) $K^+\pi^-\pi^-\pi^0$, (c) $K_s\pi^-$, (d) $K_s\pi^-\pi^+\pi^-$, and (e) $K_s\pi^-\pi^0$. The distributions are fit to a Crystal Ball Line shape for the signal and an ARGUS shape obtained from the $\Delta E$ sidebands for the background. The regions between the arrows is selected for further analysis.

The $m_{\rm BC}$ distributions for all $\bar{D}^0$ and $D^-$ tagging modes are shown in Figs. 1 and 2. Table I lists the numbers of signal and background events within the signal region defined as containing 98.8% of the signal events with $m_{\rm BC}$ below the peak and 95.5% of the signal events above the peak; the interval varies from mode to mode. The numbers of tagged events are determined from fits of the $m_{\rm BC}$ distributions to a signal function plus a background shape. The signal is described by a Crystal Ball Line shape [8,9]. For the background, we fit with a shape function analogous to one first used by the ARGUS collaboration [10], which has approximately the correct threshold behavior at large $m_{\rm BC}$, except for the $\bar{D}^0 \to K^-\pi^+$ and $\bar{D}^0 \to K^-\pi^+\pi^0$ modes where we use a fourth order polynomial. For each tagging mode, the background function is first fit to a $m_{\rm BC}$ distribution that lies within an interval from 5 to 7.5 r.m.s. widths away from the peak of the $\Delta E$ distribution. We fix the shape parameters from these fits and then use these functions for background distributions in the signal fits, allowing the normalization to float.

We find $151819 \pm 487 \pm 759$ $D^-$ and $227556 \pm 617 \pm 1138$ $\bar{D}^0$ signal events that we use for further analysis. The systematic uncertainty on this number is estimated to be $\pm 0.5\%$ by varying the fitting functions.

### B. Reconstruction of $D_s^-$ Tagging Modes

At 4170 MeV the presence of the $\gamma$ from $D_s^{*-} \to \gamma D_s^-$ causes us to adopt a different procedure. If we ignore the photon and reconstruct the $m_{\rm BC}$ distribution, we obtain the distribution from Monte Carlo shown in Fig. 3. The narrow peak occurs when the reconstructed $D_s$ does not come from the $D_s^*$ decay. Thus, the method of applying narrow cuts on $m_{\rm BC}$ and $\Delta E$, used so successfully on the $\psi(3770)$, no longer works.

Instead, we insist that the $D_s^-$ candidate has momenta which satisfies the requirement $2.015 < m_{\rm BC} < 2.067$ GeV. This requirement allows for the fact that the $D_s^-$ could have been produced directly or as a result of a $D_s^{*-}$ decay to either $\gamma D_s^-$, or $\pi^0 D_s^-$ decay with a small $\sim 5.8\%$ branching fraction [6]. We then reconstruct the invariant mass of the $D_s$ candidates. The invariant mass distributions of the tagging modes we considered in this analysis are shown in Fig. 4; they are listed in Table II, where we also give the number of signal and background events. Here we use only the secondary decays $K^{*0}(890) \to K^+\pi^-$, $K^{*+}(890) \to K_S\pi^+$, $\rho^- \to \pi^-\pi^0$, $\eta \to \gamma\gamma$ and $\eta' \to \pi^+\pi^-\eta$. (More specifically, when appropriate, we require the $K\pi$ invariant mass to be within $\pm 100$ MeV of the $K^*$ mass, the $\pi^-\pi^0$ mass to be within $\pm 100$ MeV of the $\rho^-$ mass, the $\gamma\gamma$

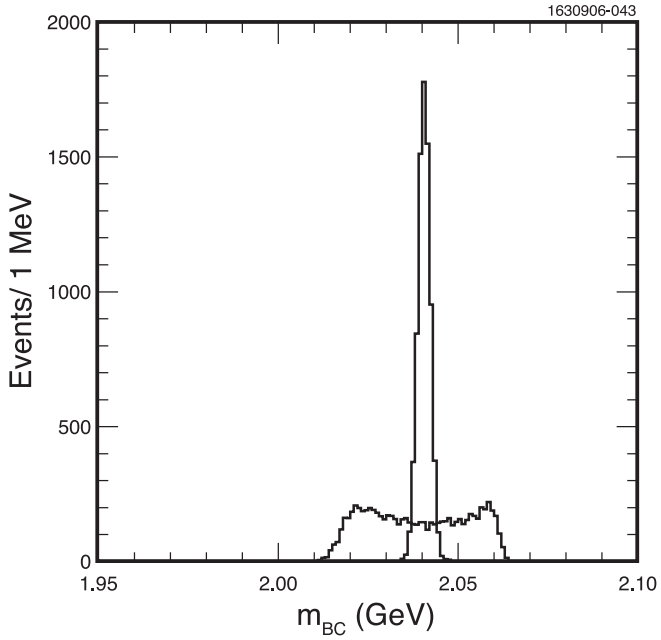


FIG. 3. The beam-constrained mass $m_{\rm BC}$ from Monte Carlo simulation of $e^+e^- \to D_s^+ D_s^{*-}$, $D_s^{*-} \to \gamma D_s^-$, $D_s^- \to \phi\pi^-$ at 4170 MeV. The narrow peak is from the $D_s^+$ and the wider one from the $D_s^-$. (The distributions are not centered at the $D_s^+$ or $D_s^{*+}$ masses, because the reconstructed particles are assumed to have the energy of the beam.)

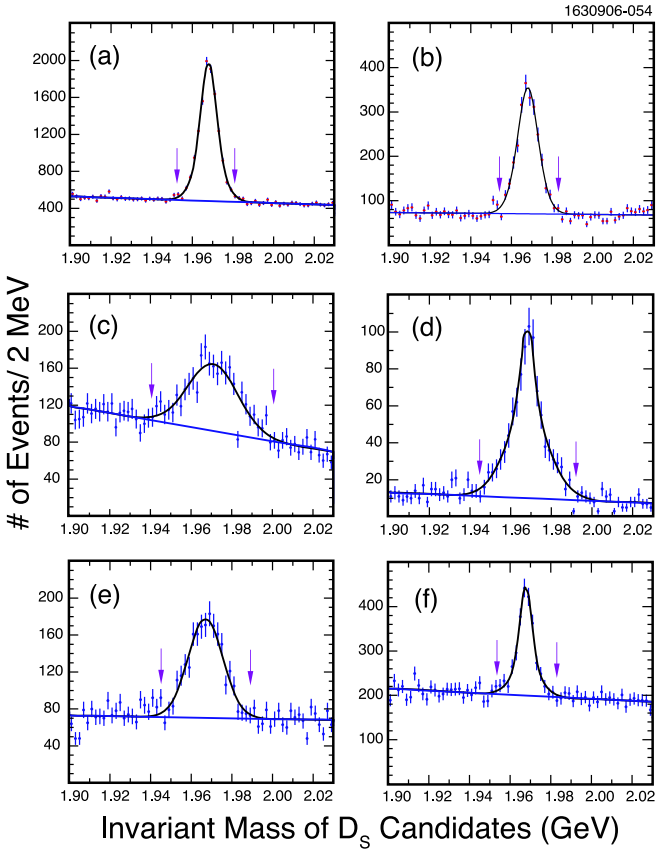


FIG. 4 (color online). Invariant mass distributions for fully reconstructed $D_s^-$ decay candidates in the final states: (a) $K^+K^-\pi^-$, (b) $K_SK^-$, (c) $\eta\pi^-$, (d) $\eta'\pi^-$, (e) $\phi\rho^-$, and (f) $K^{*0}K^{*+}$. The distributions are fit to double Gaussian signal shapes and Chebychev polynomial backgrounds. The regions between the arrows is selected for further analysis.

invariant mass minus the $\eta$ mass divided by its error to be less than 3, and the invariant mass of the $\gamma\gamma\pi^+\pi^-$ minus the $\gamma\gamma$ mass, for $\gamma\gamma$ combinations consistent with the $\eta$ hypothesis, to be within $\pm 10$ MeV of the known $\eta' - \eta$ mass difference.)

The $D_s^-$ signal regions are defined as containing 98.8% of the signal events within an invariant mass window symmetric about the $D_s^-$ mass peak. The intervals vary from mode to mode. To find the numbers of signal tag events, the invariant mass distributions are fit to a sum of two Gaussian signal functions with the means constrained to be the same and the r.m.s. widths allowed to float. The background function is a second or third order Chebychev polynomial.

We have $14522 \pm 218 \pm 145$ $D_s^-$ signal events that we use for further analysis. The systematic uncertainty is estimated to be $\pm 1.0\%$ by varying the signal and background fitting functions.

## III. $\eta$, $\eta'$ AND $\phi$ SELECTION

For the $\eta$ we use the $\gamma\gamma$ final state, which has a measured branching fraction of $(39.43 \pm 0.26)\%$. To detect $\eta'$ we use the $\pi^+\pi^-\eta$ final state, which has a branching fraction of $(44.3 \pm 1.5)\%$, with the $\eta$ subsequently decaying into $\gamma\gamma$. For the $\phi$ we use the $K^+K^-$ final state with a rate of $(49.1 \pm 0.6)\%$ [6].

The track selection and particle identification requirements for the signal side are identical to those for the tag side, except for momenta less than 0.2 GeV/$c$, where we loosen the $dE/dx$ consistency requirement to $4\sigma_K$. This is the case for both $D$ and $D_s$ meson tags.

We accept photons only in the best-resolution region of the detector, $|\cos\theta| < 0.8$, where $\theta$ is the angle of the photon with respect to the beam direction. Photon candidates must not be matched to charged tracks, must have a reconstructed energy greater than 30 MeV and have a spatial distribution in the crystals consistent with that of an electromagnetic shower.

Candidates for $\eta'$ mesons are selected by combining $\eta$ candidates within 3 r.m.s. widths of the $\eta$ mass, with a $\pi^+$ and a $\pi^-$. The mass difference between $\eta\pi^+\pi^-$ and $\eta$ is then examined. Both pions forming $\eta'$ and kaons forming $\phi$ candidates are required to pass the track selection and particle identification requirements. The signal yield is then extracted from fits to the $\eta$, $\eta' - \eta$, and $\phi$ mass distributions.

## IV. RECONSTRUCTION EFFICIENCIES

The reconstruction efficiencies for $\eta$, $\eta'$ and $\phi$ in our tag samples of $D$ and $D_s$ events are shown in Fig. 5. They are determined from a Monte Carlo simulation of the detector [11]. There is no observable difference in the efficiencies for $D^0$ and $D^+$ decays. In the case of the $D_s$, the reconstruction efficiency, especially for the $\phi$, is lower in the highest momentum bin, due to the different angular distributions of these particles, caused by the different production angles with respect to the beam of charmed mesons from $D\bar{D}$ production compared with $D_s^*\bar{D}_s$ production. In other words, the kaons on average are produced closer to the beam axis in $D_s^*\bar{D}_s$ events than in $D\bar{D}$ events.

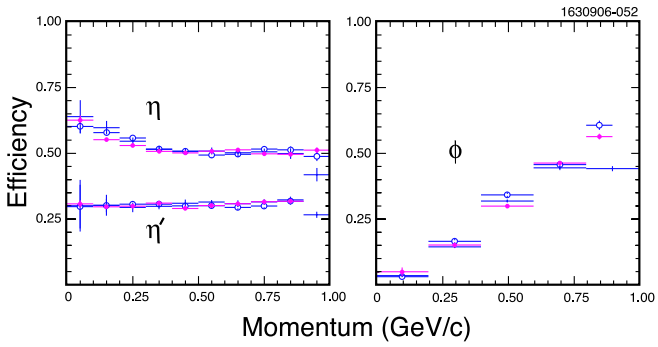


FIG. 5 (color online). Reconstruction efficiencies for: $\eta \to \gamma\gamma$, $\eta' \to \eta\pi^+\pi^-$, and $\phi \to K^+K^-$. The filled circles indicate $D^0\bar{D}^0$ events, the open circles $D^+D^-$ events, and the crosses $D_s^*\bar{D}_s$ events. The efficiencies do not include branching ratios.

The $\eta$ efficiency falls slowly below 300 MeV/$c$, and then levels out. Since our aim here is to measure the inclusive branching fractions, we break the $\eta$ sample into two parts, one below 300 MeV/$c$ and the other above. For the $\eta'$, the efficiency is constant with momentum, so we do not separate the data into momentum intervals. The $\phi$ efficiency, on the other hand, changes drastically with momentum and therefore we use several momentum regions. The increase in the $\phi$ efficiency is easily explained by the fact that as the $\phi$ becomes more energetic it is less likely to produce a kaon of $p < 0.2$ GeV/c, which would cause the event to be rejected.

The simulated $\phi$ efficiency could be inaccurate if the $\phi$ polarization were not correct; this could occur because of a poor choice of the mixture of final states. The data and Monte Carlo, however, show the same polarization. (The observed polarization is almost independent of momentum in both data and Monte Carlo.)

## V. SIGNAL YIELDS AND BRANCHING FRACTIONS

The signal yields in this analysis are evaluated by taking the difference between the $\eta$, $\eta'$ and $\phi$ yields opposite selected tags and the yields in samples that estimate the background under the tag peaks. Our procedure is somewhat different for $D$ and $D_s$ decays. In the $D$ case, we evaluate the background yields using events in the low and high sidebands of the $\Delta E$ distribution from $5\sigma$ to $7.5\sigma$ away from the peak. These sidebands are normalized to have the same number of events as the backgrounds under the $\Delta E$ peaks. In the $D_s$ case we select sidebands in the same interval relative to the peak as for the $D$ but in invariant mass rather than in $\Delta E$.

### A. Inclusive $\eta$ Yields

In Fig. 6 we show the two-photon invariant mass in our two momentum intervals for both signal and sideband regions for $D$ tags; Fig. 7 shows the corresponding distributions for $D_s$ tags.

The $\eta$ signal and background yields are determined by fits to a Crystal Ball function, to account for the peak and the low mass tail, and a background polynomial. For the signal $D^0$ region, the four fit parameters describing the Crystal Ball line shape, three for shape and one for the mean are allowed to float. These parameters are then fixed and used for the $D^0$ sideband regions and the $D^+$ and $D_s^+$ signal and sideband regions, since some of these have relatively small yields. Table III lists the yields, the efficiencies, and the branching fractions for the two momentum intervals. (Yields in the highest momentum bin include a small number of events that slightly exceed 1 GeV/$c$.)

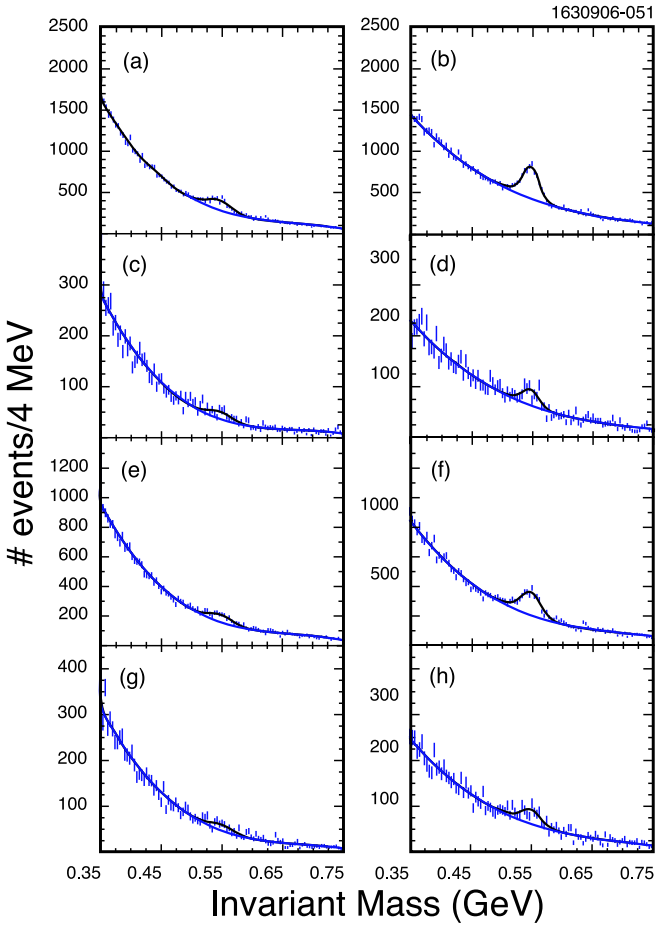


FIG. 6 (color online). Invariant mass of the $\eta \to \gamma\gamma$ candidates from $D^0$ decay: (a) signal region events with the momentum of $\eta$, $|p_\eta|$, less than 0.3 GeV/$c$, (b) signal region events with $0.3 < |p_\eta| < 1.0$ GeV/$c$, (c) sideband events with $|p_\eta| <$ 0.3 GeV/$c$, (d) sideband events with $0.3 < |p_\eta| < 1.0$ GeV/$c$. Candidates from $D^+$ decay are shown in (e)-(h), with corresponding descriptions.

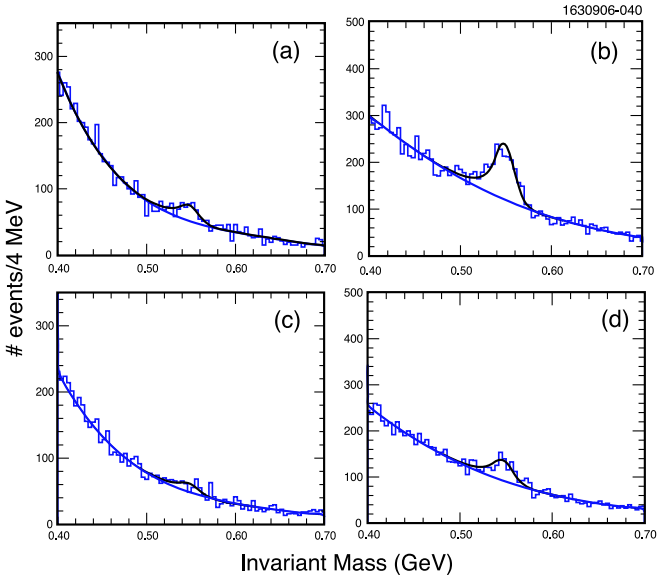


FIG. 7 (color online). Invariant mass of the $\eta \to \gamma\gamma$ candidates from $D_s^+$ decay: (a) signal region events with the momentum of $\eta$, $|p_\eta|$, less than 0.3 GeV/$c$, (b) signal region events with $0.3 < |p_\eta| < 1.0$ GeV/$c$, (c) sideband events with $|p_\eta| <$ 0.3 GeV/$c$, (d) sideband events with $0.3 < |p_\eta| < 1.0$ GeV/$c$.

The systematic uncertainties arise from several sources. For the $\eta$ we estimate a detection efficiency error of $\pm 2\%$ per photon[1] for a total of $\pm 4\%$. We also include an error due to fitting the Monte Carlo samples. In addition, there is an uncertainty caused by using the efficiency in only two momentum intervals, due to possible variations in these intervals, amounting to 3%. This error is estimated by considering the effects of different parent momentum distributions. The uncertainties on the tag yields are derived by varying the fitting functions. We also have significant contributions from uncertainties on the signal and background fitting function, determined by varying the functions. All the systematic error contributions are listed in Table IV. For the $\eta'$ and $\phi$ modes we also list the estimated uncertainties for finding the charged tracks and identifying their species. These differ somewhat between the $\eta'$ and $\phi$ because of the different track momenta involved. For the $\phi$ mode we include another additional error source due the lack of efficiency in the first momentum bin that we will discuss in more detail subsequently.

For the $\eta$ rates we find

$$\mathcal{B}(D^0 \to \eta X) = (9.5 \pm 0.4 \pm 0.8)\%$$
$$\mathcal{B}(D^+ \to \eta X) = (6.3 \pm 0.5 \pm 0.5)\%$$
$$\mathcal{B}(D_s^+ \to \eta X) = (23.5 \pm 3.1 \pm 2.0)\%.$$

Note that these rates naturally include cascade decays from $\eta' \to \eta X$.

[1]This is determined from a study of pions in $\psi(2S) \to J/\psi\pi^0\pi^0$ transitions [12].

TABLE III. $\eta$ signal yields ($N_\eta^{\rm sig}$), background yields ($N_\eta^{\rm bkg}$) and background-subtracted yields ($N_\eta$) as a function of momentum. Also listed are the $\eta$ reconstruction efficiencies ($\epsilon^i$) in percent, and the partial branching fractions versus momentum. (Yields in the highest momentum bin include a small number of events that slightly exceed 1 GeV/$c$.)

| Tag | $\lvert p_\eta\rvert$ (GeV/$c$) | $N_\eta^{\rm sig}$ | $N_\eta^{\rm bkg}$ | $N_\eta$ | $\epsilon^i$ | $\mathcal{B}^i(D\to\eta X)$ (%) |
|---|---|---|---|---|---|---|
| $D^0$ | 0.0–0.3 | 1454 ± 133 | 176 ± 33 | 1278 ± 137 | 57 | 2.5 ± 0.3 |
| | 0.3–1.0 | 3427 ± 137 | 242 ± 36 | 3185 ± 141 | 50 | 7.0 ± 0.3 |
| Sum | | 4880 ± 191 | 418 ± 49 | 4463 ± 197 | ··· | 9.5 ± 0.4 |
| $D^+$ | 0.0–0.3 | 608 ± 65 | 153 ± 35 | 455 ± 74 | 58 | 1.3 ± 0.2 |
| | 0.3–1.0 | 1811 ± 115 | 294 ± 39 | 1517 ± 121 | 51 | 5.0 ± 0.4 |
| Sum | | 2419 ± 132 | 448 ± 332 | 1972 ± 142 | ··· | 6.3 ± 0.5 |
| $D_s^+$ | 0.0–0.3 | 230 ± 38 | 152 ± 36 | 78 ± 53 | 55 | 2.5 ± 1.7 |
| | 0.3–1.0 | 963 ± 56 | 367 ± 48 | 596 ± 74 | 50 | 21.0 ± 2.6 |
| Sum | | 1193 ± 68 | 519 ± 60 | 674 ± 91 | ··· | 23.5 ± 3.1 |

TABLE IV. Systematic uncertainties ( ± ) on the inclusive $\eta$, $\eta'$ and $\phi$ branching ratios.

| Systematic uncertainties | $\eta$ (%) | $\eta'$ (%) | $\phi$ (%) |
|---|---|---|---|
| Photon reconstruction | 4.0 | 4.0 | ··· |
| Charged track finding | ··· | 1.4 | 5.0 |
| Particle identification | ··· | 2.0 | 2.0 |
| Monte Carlo fitting | 2.0 | 1.0 | 1.0 |
| Average efficiency | 3.0 | 3.2 | ··· |
| Number of tags ($D^0$ & $D^+$) | 0.5 | 0.5 | 0.5 |
| Number of tags ($D_s^+$) | 1.0 | 1.0 | 1.0 |
| Signal & Background Fitting | 6.5 | 5.3 | 2.1 |
| Estimate of 1st $p$ bin ($D^0$ & $D^+$) | ··· | ··· | 2.0 |
| Estimate of 1st $p$ bin ($D_s^+$) | ··· | ··· | 3.1 |
| Total ($D^0$ & $D^+$) | 8.5 | 8.6 | 6.3 |
| Total ($D_s^+$) | 8.5 | 8.6 | 6.8 |

### B. Inclusive $\eta'$ Yields

We first reconstruct $\gamma\gamma$ invariant mass as shown above. Then we use $\gamma\gamma$ mass combinations within $\pm 3\sigma$ of the $\eta$ mass as $\eta$ candidates, where $\sigma$ is the r.m.s. width of the mass peak. In Figs. 8 and 9 we show the $\eta\pi^+\pi^-$-$\eta$ mass difference for $D$ and $D_s$ tags from both signal and sideband regions. To determine the yields in this case we fit to a Gaussian signal function and a background polynomial. The signal shapes and means are allowed to float for the signal distributions and fixed to the values obtained there in the corresponding sideband regions.

The signal, background, and background-subtracted yields, the detection efficiency and the branching fraction are given in Table V. The systematic error sources are listed in Table IV. For the charged tracks we estimate a systematic error of $\pm 0.7\%$ for track finding[2] and $\pm 1\%$ for particle identification.

[2]This is determined from a study of pions in $\psi(2S)\to J/\psi\pi^+\pi^-$ transitions [12] but increased to account for the contribution from low momentum tracks.

### C. Inclusive $\phi$ Yields

In Figs. 10–15 we show the $K^+K^-$ invariant mass for the signal region in five different momentum intervals from both signal and sideband regions for $D^0$, $D^+$ and $D_s^+$ tags, respectively. The signals are fit with a sum of two Gaussian shapes and the background is fit to a polynomial. The signal shapes are fixed to the values obtained by Monte Carlo simulation, while the mean is allowed to float. The signal, background, and background-subtracted yields, the detection efficiency and the branching fraction in each momentum interval are given in Table VI. For $D^0$ and $D^+$

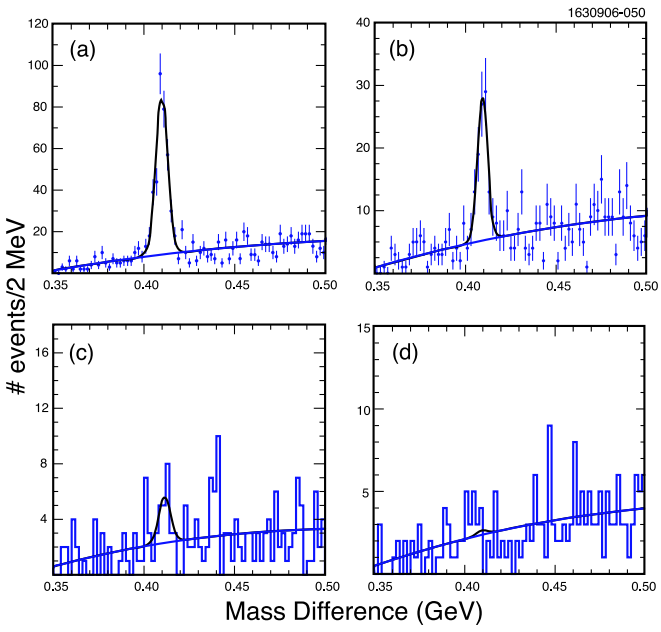


FIG. 8 (color online). Difference in the invariant mass of $\eta'\to\eta\pi^+\pi^-$ and $\eta$ ($\eta\to\gamma\gamma$) candidates from: (a) $D^0$ signal region events (b) $D^+$ signal region events (c) $D^0$ sideband events, and (d) $D^+$ sideband events. The fits are described in the text.

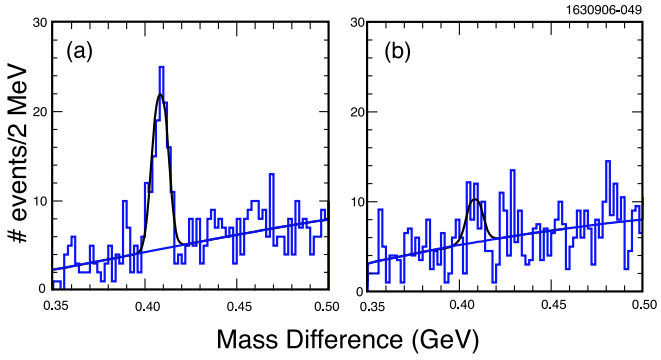


FIG. 9 (color online). $\eta\pi^+\pi^-$-$\eta$ mass difference from $D_s^+ D_s^-$ signal events (a) and sideband events (b). The fits are described in the text.

TABLE V. $\eta'$ signal yields ($N_{\eta'}^{\rm sig}$), background yields ($N_{\eta'}^{\rm bkg}$) and background-subtracted yields ($N_{\eta'}$), the $\eta'$ reconstruction efficiencies ($\epsilon^i$), and the branching fractions.

| Tag | $N_{\eta'}^{\rm sig}$ | $N_{\eta'}^{\rm bkg}$ | $N_{\eta'}$ | $\epsilon^i$ | $\mathcal{B}(D_{(s)} \to \eta' X)(\%)$ |
|---|---|---|---|---|---|
| $D^0$ | $313 \pm 20$ | $14 \pm 5$ | $299 \pm 21$ | 30 | $2.48 \pm 0.17 \pm 0.21$ |
| $D^+$ | $83 \pm 12$ | $1^{+4}_{-1}$ | $82 \pm 13$ | 30 | $1.04 \pm 0.16 \pm 0.09$ |
| $D_s^+$ | $91 \pm 12$ | $23 \pm 8$ | $68 \pm 15$ | 31 | $8.7 \pm 1.9 \pm 0.8$ |

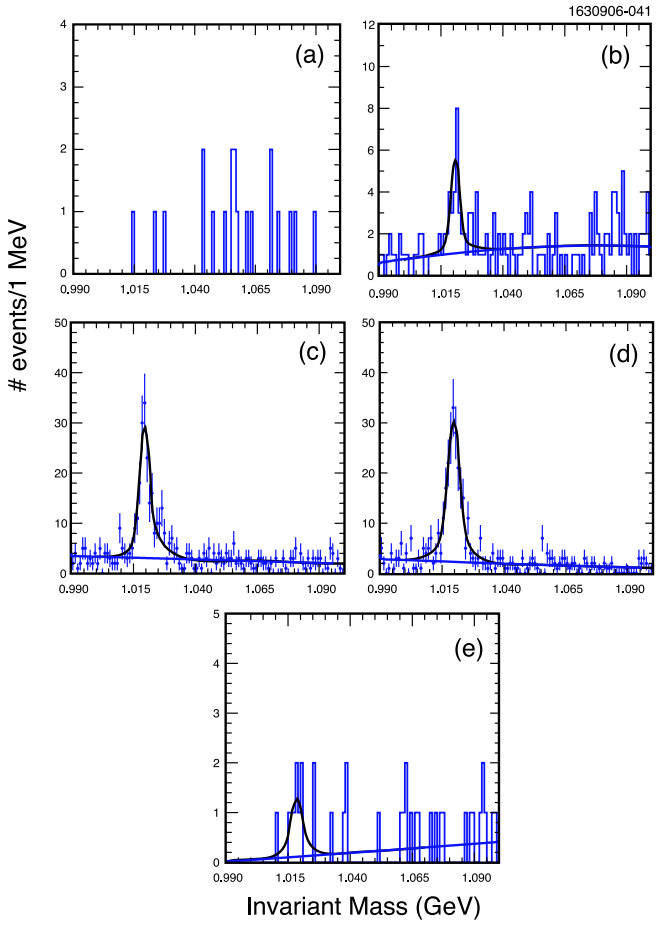


there are no events above 0.9 GeV/$c$, while for the $D_s^+$ there are a small number of events above 1.0 GeV/$c$.

Although the measured yields in the lowest momentum bin, $0 < p < 0.2$ GeV/$c$, are quite small, so are the efficiencies. To take into account possible incorrect efficiency estimates in this difficult kinematic region we make an independent estimate of the rate by using the Monte Carlo predicted fraction of the $\phi$ yield. We then take a conservative 100% error on these estimates. The fractions are 2.0%, 2.0% and 3.1%, for $D^0$, $D^+$ and $D_s^+$, respectively. These correspond to partial branching fractions of $(0.02 \pm 0.02)\%$, $(0.02 \pm 0.02)\%$, and $(0.5 \pm 0.5)\%$, respectively. Using these more reliable estimates for the rates in the first bin, we show the efficiency corrected momentum distributions in Fig. 16. The inclusive branching ratios are

$$\begin{aligned} \mathcal{B}(D^0 \to \phi X) &= (1.05 \pm 0.08 \pm 0.07)\% \\ \mathcal{B}(D^+ \to \phi X) &= (1.03 \pm 0.10 \pm 0.07)\% \\ \mathcal{B}(D_s^+ \to \phi X) &= (16.1 \pm 1.2 \pm 1.1)\%. \end{aligned} \tag{3}$$

The systematic uncertainties are listed in Table IV. Because of the difficulty in tracking slow charged kaons, we use an increased systemic error of $\pm 2.5\%$ per track in evaluating the efficiency error from track finding. The error due to particle identification remains at $\pm 1\%$.

FIG. 10 (color online). Invariant mass of $\phi \to K^+K^-$ candidates from $D^0\bar{D}^0$ signal events in five different momentum intervals: (a) $0 < |p_\phi| < 0.2$ GeV/$c$, (b) $0.2 < |p_\phi| < 0.4$ GeV/$c$, (c) $0.4 < |p_\phi| < 0.6$ GeV/$c$, (d) $0.6 < |p_\phi| < 0.8$ GeV/$c$, (e) $0.8 < |p_\phi| < 0.9$ GeV/$c$. The fits are described in the text.

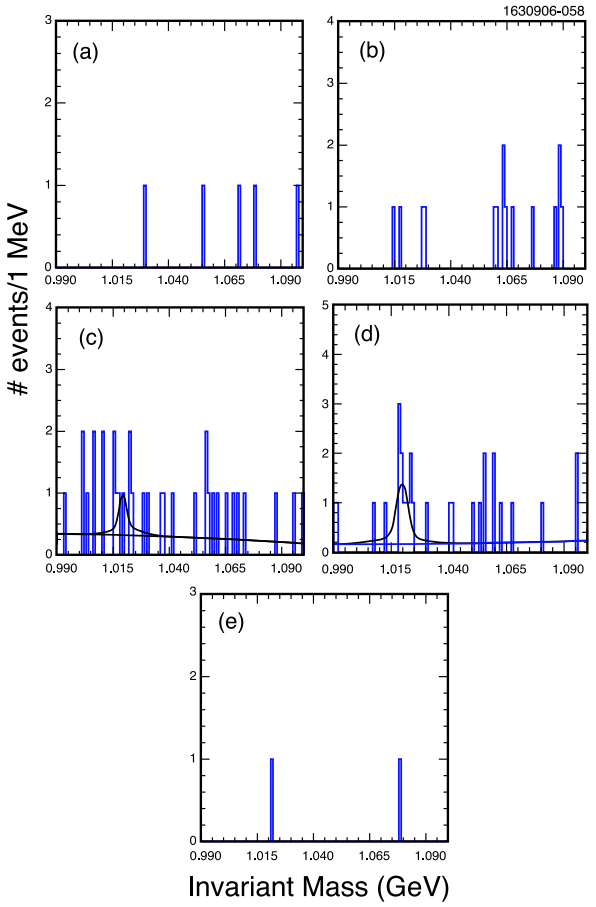


FIG. 11 (color online). Invariant mass of $\phi \to K^+K^-$ candidates from $D^0\bar{D}^0$ background events in five different momentum intervals: (a) $0 < |p_\phi| < 0.2$ GeV/$c$, (b) $0.2 < |p_\phi| < 0.4$ GeV/$c$, (c) $0.4 < |p_\phi| < 0.6$ GeV/$c$, (d) $0.6 < |p_\phi| < 0.8$ GeV/$c$, (e) $0.8 < |p_\phi| < 0.9$ GeV/$c$. The fits are described in the text.

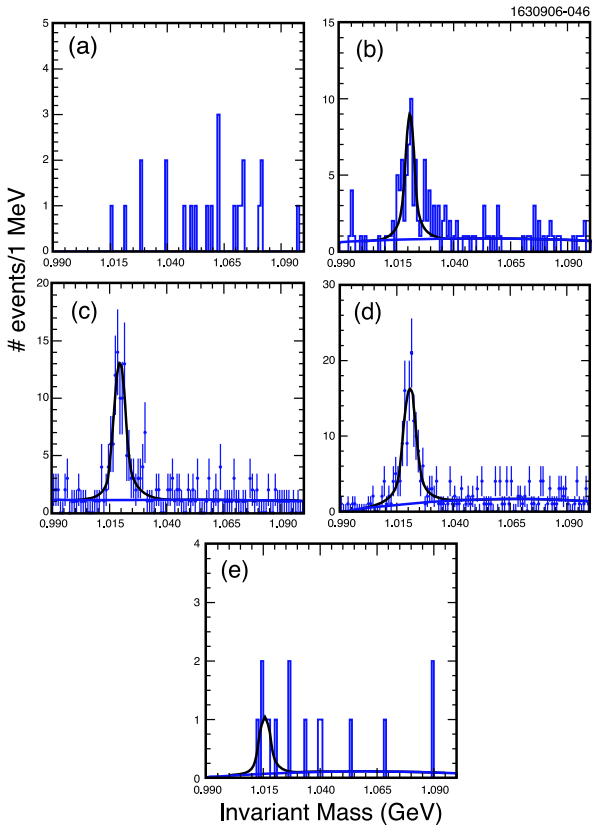


FIG. 12 (color online). Invariant mass of $\phi \to K^+K^-$ candidates from $D^+D^-$ signal events in five different momentum intervals: (a) $0 < |p_\phi| < 0.2$ GeV/$c$, (b) $0.2 < |p_\phi| < 0.4$ GeV/$c$, (c) $0.4 < |p_\phi| < 0.6$ GeV/$c$, (d) $0.6 < |p_\phi| < 0.8$ GeV/$c$, (e) $0.8 < |p_\phi| < 0.9$ GeV/$c$. The fits are described in the text.

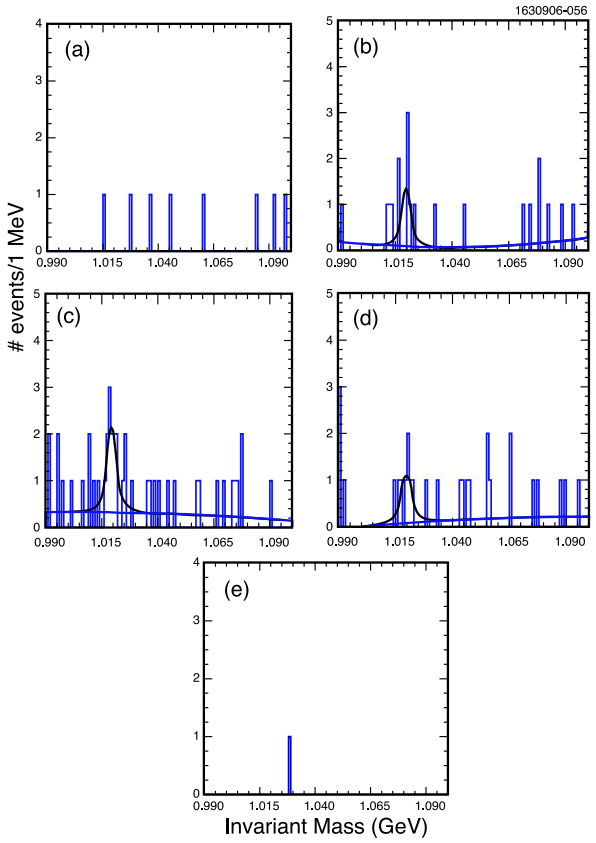


FIG. 13 (color online). Invariant mass of $\phi \to K^+K^-$ candidates from $D^+D^-$ background events in five different momentum intervals: (a) $0 < |p_\phi| < 0.2$ GeV/$c$, (b) $0.2 < |p_\phi| < 0.4$ GeV/$c$, (c) $0.4 < |p_\phi| < 0.6$ GeV/$c$, (d) $0.6 < |p_\phi| < 0.8$ GeV/$c$, (e) $0.8 < |p_\phi| < 0.9$ GeV/$c$. The fits are described in the text.

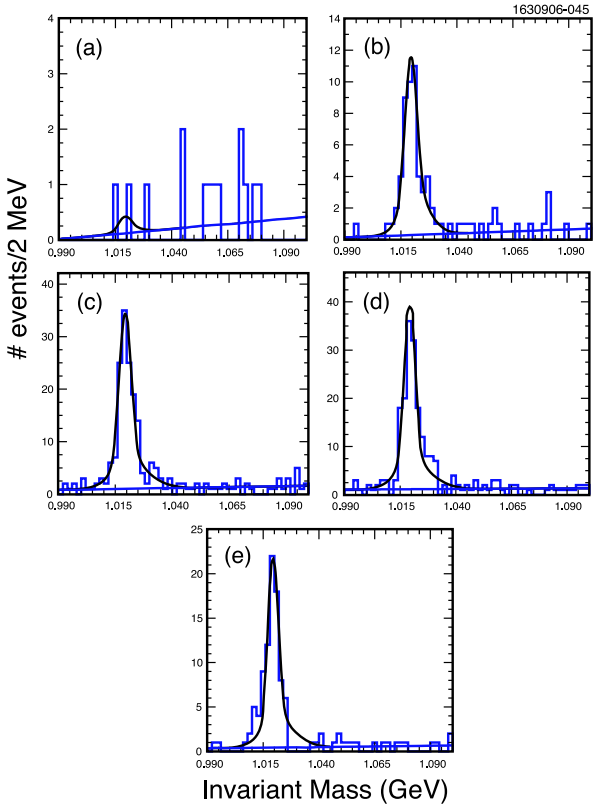


FIG. 14 (color online). Invariant mass of $\phi \to K^+K^-$ candidates from $D_s^+D_s^-$ signal events in five different momentum intervals: (a) $0 < |p_\phi| < 0.2$ GeV/$c$, (b) $0.2 < |p_\phi| < 0.4$ GeV/$c$, (c) $0.4 < |p_\phi| < 0.6$ GeV/$c$, (d) $0.6 < |p_\phi| < 0.8$ GeV/$c$, (e) $|p_\phi| > 0.8$ GeV/$c$. The fits are described in the text.

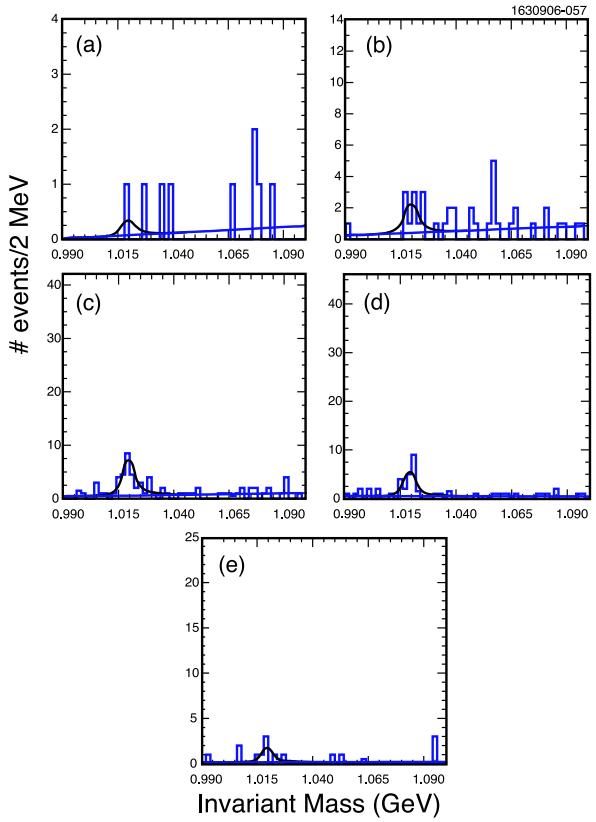


FIG. 15 (color online). Invariant mass of $\phi \to K^+K^-$ candidates from $D_s^+ D_s^-$ background events in five different momentum intervals: (a) $0 < |p_\phi| < 0.2$ GeV/$c$, (b) $0.2 < |p_\phi| < 0.4$ GeV/$c$, (c) $0.4 < |p_\phi| < 0.6$ GeV/$c$, (d) $0.6 < |p_\phi| < 0.8$ GeV/$c$, (e) $0.8 < |p_\phi|$ GeV/$c$. The fits are described in the text.

TABLE VI. Measured $\phi$ signal yields ($N_\phi^{\rm sig}$), background yields ($N_\phi^{\rm bkg}$) and background-subtracted yields ($N_\phi$) versus momentum from $D$ and $D_s$ decays. Also listed are the $\phi$ reconstruction efficiencies ($\epsilon^i$), and the partial branching fractions vs momentum. (Note that measurements in the lowest momentum interval will be replaced by a model dependent estimate.)

| $\lvert p_\phi \rvert$ (GeV/$c$) | $N_\phi^{\rm sig}$ | $N_\phi^{\rm bkg}$ | $N_\phi$ | $\epsilon^i$ (%) | $\mathcal{B}^i(D_{(s)} \to \phi X)$(%) |
|---|---|---|---|---|---|
| $D^0 \to \phi X$ | | | | | |
| 0.0–0.2 | 1.0 ± 1.0 | 1.0 ± 1.0 | 0.0 ± 1.4 | 5.2 | 0.0 ± 0.0 |
| 0.2–0.4 | 25.5 ± 7.9 | 2.0 ± 1.4 | 23.5 ± 8.0 | 15.3 | 0.14 ± 0.05 |
| 0.4–0.6 | 171.9 ± 18.1 | 3.2 ± 2.8 | 168.7 ± 18.3 | 30.2 | 0.50 ± 0.05 |
| 0.6–0.8 | 209.7 ± 17.6 | 11.3 ± 3.8 | 198.4 ± 18.0 | 46.5 | 0.38 ± 0.03 |
| 0.8–0.9 | 8.7 ± 3.5 | 1.0 ± 1.0 | 7.7 ± 3.7 | 56.6 | 0.012 ± 0.006 |
| Sum | 416.7 ± 26.7 | 18.5 ± 5.1 | 398.2 ± 27.2 | ··· | 1.03 ± 0.08 |
| $D^+ \to \phi X$ | | | | | |
| 0.0–0.2 | 3.0 ± 1.7 | 1.0 ± 1.0 | 2.0 ± 2.0 | 3.3 | 0.08 ± 0.08 |
| 0.2–0.4 | 49.9 ± 8.6 | 7.7 ± 3.3 | 42.2 ± 9.2 | 16.8 | 0.34 ± 0.07 |
| 0.4–0.6 | 90.2 ± 11.8 | 12.1 ± 4.2 | 78.2 ± 12.5 | 34.4 | 0.30 ± 0.05 |
| 0.6–0.8 | 127.6 ± 14.0 | 7.6 ± 3.0 | 119.9 ± 14.4 | 45.9 | 0.35 ± 0.04 |
| 0.8–0.9 | 6.8 ± 3.1 | 1.0 ± 1.0 | 5.8 ± 3.3 | 60.9 | 0.013 ± 0.002 |
| Sum | 277.4 ± 20.6 | 29.4 ± 6.3 | 248.0 ± 21.3 | ··· | 1.08 ± 0.12 |
| $D_s^+ \to \phi X$ | | | | | |
| 0.0–0.2 | 1.4 ± 1.6 | 1.2 ± 1.4 | 0.1 ± 2.1 | 3.7 | 0.1 ± 0.8 |
| 0.2–0.4 | 49.0 ± 7.4 | 8.3 ± 3.5 | 40.7 ± 8.2 | 14.6 | 3.9 ± 0.8 |
| 0.4–0.6 | 144.4 ± 12.9 | 28.4 ± 6.2 | 116.1 ± 14.3 | 32.1 | 5.1 ± 0.6 |
| 0.6–0.8 | 155.6 ± 13.1 | 20.3 ± 5.1 | 135.3 ± 14.1 | 44.7 | 4.2 ± 0.5 |
| >0.8 | 82.1 ± 9.1 | 6.3 ± 3.0 | 75.8 ± 9.6 | 44.4 | 2.4 ± 0.3 |
| Total | 432.5 ± 21.9 | 64.5 ± 9.4 | 368.0 ± 23.8 | ··· | 15.7 ± 1.4 |

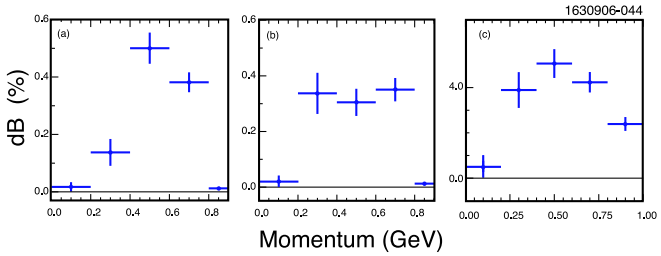


FIG. 16 (color online). The branching fraction in % in each 200 MeV interval of momentum for $\phi$ mesons from (a) $D^0$ decays, (b) $D^+$ decays and (c) $D_s^+$ decays.

TABLE VII. Summary of inclusive branching ratio results.

| Mode | $D^0$ (%) | | $D^+$ (%) | | $D_s^+$ (%) | |
|---|---|---|---|---|---|---|
| | Our result | PDG | Our result | PDG | Our result | PDG |
| $\eta X$ | $9.5 \pm 0.4 \pm 0.8$ | $<13$ | $6.3 \pm 0.5 \pm 0.5$ | $<13$ | $23.5 \pm 3.1 \pm 2.0$ | $\cdots$ |
| $\eta' X$ | $2.48 \pm 0.17 \pm 0.21$ | $\cdots$ | $1.04 \pm 0.16 \pm 0.09$ | $\cdots$ | $8.7 \pm 1.9 \pm 0.8$ | $\cdots$ |
| $\phi X$ | $1.05 \pm 0.08 \pm 0.07$ | $1.7 \pm 0.8$ | $1.03 \pm 0.10 \pm 0.07$ | $<1.8$ | $16.1 \pm 1.2 \pm 1.1$ | $\cdots$ |

TABLE VIII. Ratios of $D_s^+$ to $D$ yields. Common systematic errors have been eliminated.

| Ratio | $\eta$ | $\eta'$ | $\phi$ |
|---|---|---|---|
| $D_s^+/D^0$ | $2.47 \pm 0.34 \pm 0.18$ | $3.51 \pm 0.80 \pm 0.27$ | $15.3 \pm 1.6 \pm 0.8$ |
| $D_s^+/D^+$ | $3.73 \pm 0.57 \pm 0.27$ | $8.37 \pm 2.23 \pm 0.64$ | $15.6 \pm 1.9 \pm 0.8$ |

## VI. CONCLUSIONS

Our results of the inclusive $\eta$, $\eta'$ and $\phi$ production rates from $D^0$, $D^+$ and $D_s^+$ decays are summarized in Table VII. Of the 9 measured rates in this paper, 8 are first measurements and the other one, $D^0 \to \phi X$, improves the accuracy from 50% to 10%. We are consistent with previous upper limits [6] in the three cases where they exist.

These particles all have significant components of $s\bar{s}$. Our results show that $\eta'$ and $\phi$ are relatively rare in $D^0$ and $D^+$ decay while the $\eta$ which has a lower mass and a significant light quark component, is produced at a significantly higher rate. The $\eta$, $\eta'$ and $\phi$ are all produced at higher rates in $D_s$ decays than the corresponding rates from $D$ decays. The ratio of rates is given in Table VIII. The $\phi$ yield is 15 times higher in $D_s^+$ decays than in $D$ decays.

The large asymmetry in the yields of these particles between $D_s$ and the lighter $D$ mesons will permit further studies of $B_s$ decays at the $\Upsilon(5S)$, and will be most useful for separating $B_s$ from $B$ decays at hadron colliders.

## ACKNOWLEDGMENTS

We gratefully acknowledge the effort of the CESR staff in providing us with excellent luminosity and running conditions. D. Cronin-Hennessy and A. Ryd thank the A. P. Sloan Foundation. This work was supported by the National Science Foundation, the U.S. Department of Energy, and the Natural Sciences and Engineering Research Council of Canada.

[1] M. Artuso *et al.* (CLEO), Phys. Rev. Lett. **95**, 261801 (2005); G. Huang *et al.* (CLEO), hep-ex/0607080.
[2] R. Poling, hep-ex/0606016.
[3] Y. Kubota *et al.* (CLEO), Nucl. Instrum. Methods Phys. Res., Sect. A **320**, 66 (1992).
[4] D. Peterson *et al.*, Nucl. Instrum. Methods Phys. Res., Sect. A **478**, 142 (2002).
[5] M. Artuso *et al.*, Nucl. Instrum. Methods Phys. Res., Sect. A **502**, 91 (2003).
[6] W.-M. Yao *et al.*, J. Phys. G **33**, 1 (2006).
[7] M. Artuso *et al.* (CLEO Collaboration), Phys. Rev. Lett. **95**, 251801 (2005).
[8] T. Skwarnicki, DESY, Report No. DESY F31-86-02 1986 (unpublished).
[9] P. Rubin *et al.* (CLEO), Phys. Rev. D **73**, 112005 (2006).
[10] The function is $f(m_{\rm BC}) = A(m_{\rm BC} + B) \times \sqrt{1 - (\frac{m_{\rm BC}+B}{C})^2} e^{D(1-[(m_{\rm BC}+B)/C]^2)}$. Here $A$ is the overall normalization and $B$, $C$ and $D$ are parameters that govern the

shape. See H. Albrecht *et al.* (ARGUS), Phys. Lett. B **229**, 304 (1989).

[11] D. J. Lange, Nucl. Instrum. Methods Phys. Res., Sect. A **462**, 152 (2001); R. Brun *et al.* (Geant 3.21), CERN Program Library Long Writeup W5013, 1993 (unpublished); For final state photon radiation see E. Barberio, B. van Eijk, Z. Was, Comput. Phys. Commun. **66**, 115 (1991); E. Barberio and Z. Was, Comput. Phys. Commun. **79**, 291 (1994).

[12] N. E. Adam *et al.* (CLEO), hep-ex/0607079.